

Buckling analysis of imperfect I-section beam-columns with stochastic shell finite elements

Dominik Schillinger · Vissarion Papadopoulos ·
Manfred Bischoff · Manolis Papadrakakis

Received: 3 September 2009 / Accepted: 28 February 2010 / Published online: 8 April 2010
© Springer-Verlag 2010

Abstract Buckling loads of thin-walled I-section beam-columns exhibit a wide stochastic scattering due to the uncertainty of imperfections. The present paper proposes a finite element based methodology for the stochastic buckling simulation of I-sections, which uses random fields to accurately describe the fluctuating size and spatial correlation of imperfections. The stochastic buckling behaviour is evaluated by crude Monte-Carlo simulation, based on a large number of I-section samples, which are generated by spectral representation and subsequently analyzed by non-linear shell finite elements. The application to an example I-section beam-column demonstrates that the simulated buckling response is in good agreement with experiments and follows key concepts of imperfection triggered buckling. The derivation of the buckling load variability and the stochastic interaction curve for combined compression and major axis bending as well as stochastic sensitivity studies for thickness and geometric imperfections illustrate potential benefits of the proposed methodology in buckling related research and applications.

D. Schillinger (✉)
Lehrstuhl für Computation in Engineering, Technische Universität München, Arcisstr. 21, 80333 Munich, Germany
e-mail: schillinger@bv.tum.de

V. Papadopoulos · M. Papadrakakis
Institute of Structural Analysis and Seismic Research,
National Technical University of Athens, 9 Iroon Polytechniou,
15780 Athens, Greece
e-mail: papado@central.ntua.gr

M. Papadrakakis
e-mail: mpapadra@central.ntua.gr

M. Bischoff
Institut für Baustatik und Baudynamik, Universität Stuttgart,
Pfaffenwaldring 7, 70550 Stuttgart, Germany
e-mail: bischoff@ibb.uni-stuttgart.de

Keywords Buckling of I-section beam-columns · Stochastic shell finite elements · Random field based imperfections · Spectral representation · Evolutionary power spectra · Method of separation

1 Introduction

Imperfections in thin-walled I-sections denote small variations of geometry and material parameters from their nominal values, which result from random events during industrial manufacturing, transportation and on-site assembly [7,47]. Thin-walled structures such as I-section members typically exhibit a detrimental imperfection sensitivity, which drastically reduces their ultimate load bearing capacity compared to their theoretical strength [8,9,33]. Additionally, the uncertainty of imperfections leads to a stochastic variability of buckling loads in nominally identical members [15,47]. The standard simulation approach for imperfection triggered buckling assumes imperfections in the form of the critical Eigenmode of the perfect structure [34,47], whose amplitude can additionally be modulated by a random variable to include the aspect of uncertainty [18,22,35]. A more sophisticated approach based on a random field formulation of imperfections has been extensively applied for the stochastic buckling analysis of thin-walled cylindrical shells, using either spectral representation of random fields [4,25–29,42] or the Karhunen-Loève expansion [12,36–38]. Random field based imperfection modeling has also been recently applied to a broader range of structures, such as beams, plates, frames and arches [6,11,23,46].

Against this background, the paper at hand proposes the adoption of random fields for modeling geometric and thickness imperfections in I-sections. A random field represents an ensemble of spatial functions, whose exact values are

a-priori indeterminate, but follow a probability distribution and a correlation function [24,30,48]. Random fields are thus able to describe the spatial variability of imperfections without relying on the standard Eigenmode concept. The imperfection model considered is a combination of several homogeneous and evolutionary Gaussian random fields that account for the specific characteristics of local and global geometric as well as thickness imperfections. Its stochastics, in terms of random shapes and amplitudes, are characterized by power spectra [31,32], which are calibrated from series of imperfection measurements by power spectrum estimation techniques [30,39,48]. For the accurate estimation of evolutionary power spectra, the recently proposed method of separation is applied [39], which combines accurate spectrum resolution in space with an optimum localization in frequency and can thus reliably handle the strong narrow-bandedness of imperfection measurements. With known power spectra, an arbitrary number of imperfect I-section samples can be generated by spectral representation [40,41,43]. The samples are discretized with the natural mode based triangular shell element TRIC [1–3,5] and the stochastic behaviour of the system at ultimate strength is determined by geometrically and materially non-linear FE analyses in conjunction with a crude Monte-Carlo approach.

The proposed methodology is illustrated for a realistic example of a short-length I-section beam-column, for which a large-scale imperfection database is available [19]. The simulated buckling behaviour of the imperfect I-section member is first assessed from physical, experimental and stochastic points of view. Sensitivity studies for geometric and thickness imperfections are then conducted to determine their relative impact on the stochastic buckling behaviour. The imperfect I-section model is finally examined under different combinations of axial compression and major axis bending to derive a stochastic interaction curve. The results demonstrate that the proposed methodology achieves a comprehensive and realistic description of the physical buckling phenomena for I-section beam-columns in terms of ultimate strength, load-displacement response, mode shapes and their stochastic variabilities.

The paper is organized as follows: Section 2 briefly discusses aspects of the stochastic finite element method. Section 3 deals with conceptual modeling of imperfections using random fields. Section 4 illustrates the corresponding finite element discretization. In Sect. 5, numerical results of the proposed methodology are presented for the I-section beam-column example.

2 Basic elements of stochastic FEM

Stochastic finite element techniques combine deterministic FEM with stochastic strategies from reliability analysis, signal processing and probability theory [14,37,44,45].

Some basic background principles of the methods used in this study are provided in the following.

2.1 The non-linear shell finite element TRIC

The finite element computations are performed with the multi-layered, shear-deformable triangular facet shell element TRIC, which is based on the natural mode method [1]. It has been proven to be robust, locking-resistant and cost-effective for nonlinear analysis of thin and moderately thick isotropic as well as composite plate and shell structures [2,3,5]. The TRIC element has 18 degrees of freedom (6 per node), which lead to 12 natural straining modes generated by a projection of the Cartesian nodal displacements and rotations on the edges of the triangle. The natural stiffness matrix is derived from the statement of variation of the strain energy with respect to the natural coordinates. The geometric stiffness is based on large deflections but small strains. The elasto-plastic stiffness of the element is obtained by summing up the natural elasto-plastic stiffnesses of the element layers. The resulting non-linear system of equations is solved by the arc-length path-following method, which is able to predict reliably the full non-linear pre- and post-buckling response [3,13].

2.2 Power spectrum estimation and spectral representation

A random physical phenomenon can be simulated by spectral representation on the basis of a series of m experimental measurements that are interpreted as realizations $h^{(i)}(x)$, $i = 1, 2, \dots, m$ of the underlying random field $h(x)$ [30–32,48]. Measurements $h^{(i)}(x)$ are first divided into a deterministic mean $\mu(x)$ and zero-mean components $f^{(i)}(x)$. If the zero-mean field $f(x)$ can be assumed to be homogeneous, the corresponding power spectrum $S_h(\omega)$ can be estimated by the periodogram [30,48]

$$\tilde{S}_h(\omega) = E \left[\frac{1}{2\pi L} \cdot \left| \int_0^L f^{(i)}(x) \cdot e^{-I\omega x} dx \right|^2 \right] \quad (1)$$

where the term in absolute value is the Fourier transform of $f^{(i)}(x)$, $E[\]$ denotes the operator of mathematical expectation, L is the length of $f^{(i)}(x)$ and I is the complex unit. If the zero-mean part $f^{(i)}(x)$ of the measurements are evolutionary and can be assumed to be approximately separable, the corresponding power spectrum $S(\omega, x)$ can be estimated by the method of separation [39]

$$\tilde{S}(\omega, x) = E \left[\left| f^{(i)}(x) \right|^2 \right] \cdot \frac{\tilde{S}_h(\omega)}{2 \int_0^\infty \tilde{S}_h(\omega) d\omega} \quad (2)$$

The left hand side of Eq. (2) denotes the estimated mean square; the right hand side represents a normalization of

the periodogram based homogeneous estimate $\tilde{S}_h(\omega)$ from Eq. (1). Due to the decoupling into a spatial and a frequency part, which simultaneously allows an accurate resolution in space and an optimum localization in frequency, the method of separation Eq. (2) is especially suitable for the robust estimation of strongly narrow-band power spectra, as they are typical for geometric imperfection measurements. The complete derivation of the method of separation and a comparison with standard techniques for the estimation of different benchmark spectra has been recently presented in [39]. In particular, this study shows both analytically and numerically that for separable spectra the estimation of Eq. (2) converges to the true spectrum for an infinite number of input samples. Furthermore, it shows that the method of separation yields considerably better estimation results for strongly narrow-band imperfection samples than any standard evolutionary estimation technique.

If the power spectrum $S_h(\omega, x)$ of $f(x)$ is known, an arbitrary number m of corresponding random samples can be generated by the spectral representation method [40,41,43], which reads for a one-dimensional univariate zero-mean Gaussian random field

$$f^{(i)}(x) = \sqrt{2} \sum_{n=0}^{N-1} A_n \cos(\omega_n x + \phi_n^{(i)}) \tag{3}$$

with

$$A_n = \sqrt{2 \cdot S(\omega_n, x) \cdot \Delta\omega} \tag{4a}$$

$$\omega_n = n \cdot \Delta\omega \tag{4b}$$

$$\Delta\omega = \omega_{up}/N \tag{4c}$$

$$A_0 = 0 \vee S(\omega_0, x) = 0 \tag{4d}$$

where $i = 1, 2, \dots, m$ and $n = 0, 1, 2, \dots, (N - 1)$. The parameter ω_{up} is the cut-off frequency, beyond which the power spectrum is assumed to be zero, the integer N determines the discretization of the active frequency range, and $\phi_n^{(i)}$ denotes the i^{th} realization of N independent phase angles uniformly distributed in the range $[0, 2\pi]$. To obtain samples of the original random field $h(x)$, the deterministic mean $\mu(x)$ has to be superposed to Eq. (3).

2.3 Monte-Carlo simulation (MCS)

In the present context of I-section buckling, the general MCS strategy can be interpreted as follows:

1. Define a random field based conceptual model of an imperfect I-section member.
2. Generate m imperfect I-section realizations by spectral representation and determine the corresponding m individual buckling loads $P_{crit}^i, i = 1, 2, \dots, m$ by deterministic FE computations.

3. Evaluate the buckling load variability from the individual buckling loads $P_{crit}^i, i = 1, 2, \dots, m$.

In the present study, the load variability is described by scatter plots, histograms and stochastic key parameters mean μ , standard deviation σ and coefficient of variation $Cov = \sigma/\mu$, which represents an objective normalized measure of stochastic dispersion.

3 Conceptual modeling of an imperfect I-section

In the following, the available example database [19] is briefly presented and the random field based imperfection model and its implementation for an I-section beam-column are derived in detail.

3.1 Test specimen and imperfection measurements

The report [19] contains extensive imperfection measurements for a series of six nominally identical, 2 m long, welded I-section members as illustrated in Fig. 1. Web stiffeners and plates at the ends of the specimens enable levers to be rigidly connected for the transfer of moments. A horizontal reaction frame as shown in Fig. 2 has been used to determine the buckling loads for several load cases, which consist of pure compression, pure major-axis bending as well as combined compression and major-axis bending.

Geometric imperfections have been measured with displacement transducers at 9 cross-sectional positions in distances of 25 mm along the beam axis as shown in Fig. 1b. Since the members are assumed to be perfectly aligned in the reaction frame, the one-dimensional imperfection signals are referred to a straight line fitted through the two end point readings. The report contains five types of local imperfections, displaying directly the measurements at positions $\delta_1, \delta_3, \delta_4, \delta_5$ and δ_7 , and three global imperfections, which have been processed from the rest of the local measurements as

$$u = \frac{\delta_8 + \delta_9}{2} \tag{5a}$$

$$v = \frac{\delta_2 - \delta_6}{2} \tag{5b}$$

$$\theta = \frac{\delta_9 - \delta_8}{600 \text{ mm}} \tag{5c}$$

Parameters u, v and θ represent global cross-sectional translations in weak and strong axis directions and rotation about the cross-sectional center of gravity. A cross-correlation analysis between the eight measurement components was performed, which did not yield a systematic interdependence. Therefore, these parameters are assumed to be fully uncorrelated. Some example measurements are given in Fig. 3.

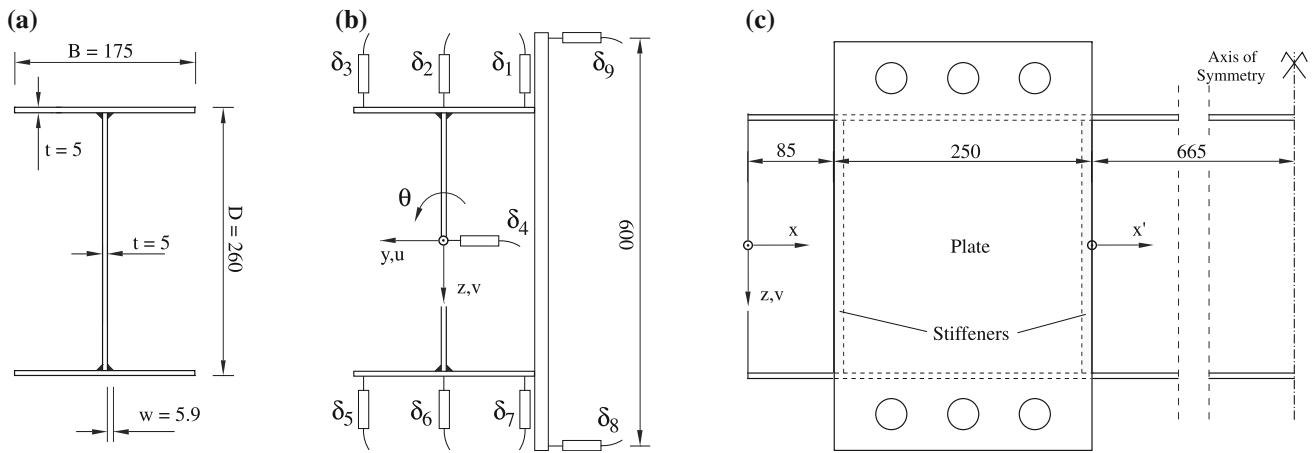
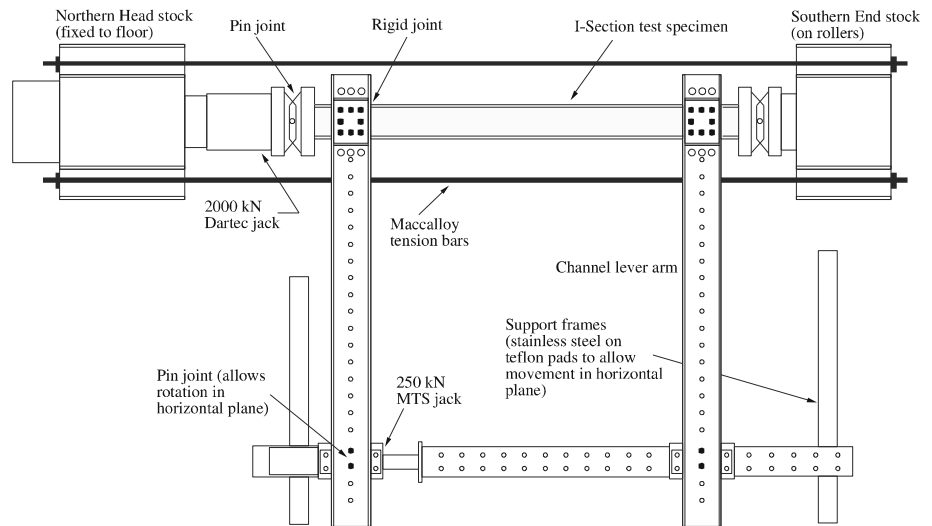


Fig. 1 The I-section test member. The total length and the free length between stiffened parts are 2000 and 1330 mm, respectively. **a** Section dimensions. **b** Displacement transducers. **c** Length dimensions, additional stiffeners and plates

Fig. 2 Reaction frame for beam-column buckling tests [19]



Thickness imperfections have been measured only locally at two different positions per specimen, from which the mean $\mu_t = 4.8842$ mm and standard deviation $\sigma_t = 0.0664$ mm can be evaluated. Material parameters show no variations within measurement accuracy and are therefore considered deterministic with: Young’s modulus $E = 2.1 \cdot 10^5$ N/mm², yield stress $\sigma_y = 400$ N/mm² and Poisson’s ratio $\nu = 0.3$. Residual stress measurements are used to calibrate a standard deterministic residual stress block model [19,47] as shown in Fig. 4, which specifies the residual normal stresses in longitudinal member direction to be superposed as a pre-stress throughout all following computations.

3.2 Geometric imperfection model

In view of available imperfection measurements, the conceptual geometric imperfection profile is defined by five local and three global components, which are illustrated in Fig. 5.

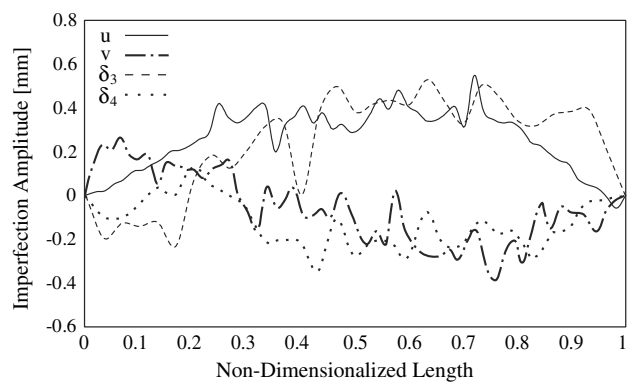


Fig. 3 Examples of measured geometric imperfections

Local imperfections λ_1 to λ_5 describe local geometric inaccuracies perpendicular to the flange and web plates in the cross-sectional plane. They are superposed to the perfect outer flange edges and web center, while the web-flange junctions

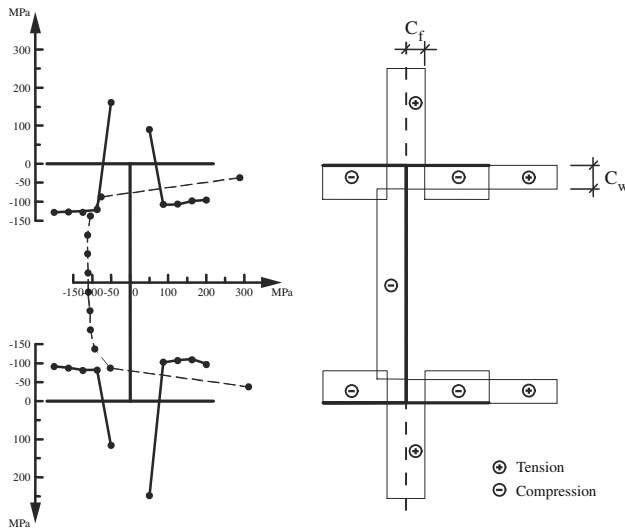


Fig. 4 Measured residual stresses (left) [19] and residual stress model (right) with $C_f = 18.11$ mm, $C_w = 25.98$ mm. Tensile and compressive stress blocks are assumed at 400 and -110 N/mm²

remain perfect. Intermediate imperfections in flanges and web are interpolated linearly and parabolically, respectively. The assumptions of fixed junctions and interpolation shapes are confirmed by measurements at intermediate plate points in similar I-sections [18]. Global imperfections γ_1 to γ_3 describe deviations from perfect alignment, i.e. weak and strong axis translations and cross-sectional rotation, which are superposed to the locally imperfect geometry.

The random field representation for local components δ_k , $k = 1, 2, 3, 4, 5$, is assumed to be zero-mean and homogeneous, so that corresponding power spectra $\tilde{S}_k(\omega)$ can be estimated by inserting measurements $\delta_1, \delta_3, \delta_4, \delta_5$ and δ_7 into the periodogram Eq. (1). The random field representation for global components γ_l , $l = 1, 2, 3$, consist of mean functions

μ_l evaluated from the corresponding series of processed measurements u, v and θ , and of the corresponding zero-mean evolutionary random fields, whose power spectra $\tilde{S}_l(\omega, x)$ are estimated by inserting the zero-mean parts of u, v and θ , into the method of separation Eq. (2). In view of Eq. (3), an arbitrary number of local and global random field samples λ_k and γ_l can then be generated by spectral representation as

$$\lambda_k^{(i)}(x) = \sqrt{2} \sum_{n=0}^{N-1} A_{k,n} \cdot \cos(\omega_n x + \phi_n^{(i)}) \tag{6a}$$

$$A_{k,n} = \sqrt{2 \cdot \tilde{S}_k(\omega_n) \cdot \Delta\omega} \tag{6b}$$

$$\gamma_l^{(i)}(x) = \mu_l + \sqrt{2} \sum_{n=0}^{N-1} A_{l,n} \cdot \cos(\omega_n x + \phi_n^{(i)}) \tag{7a}$$

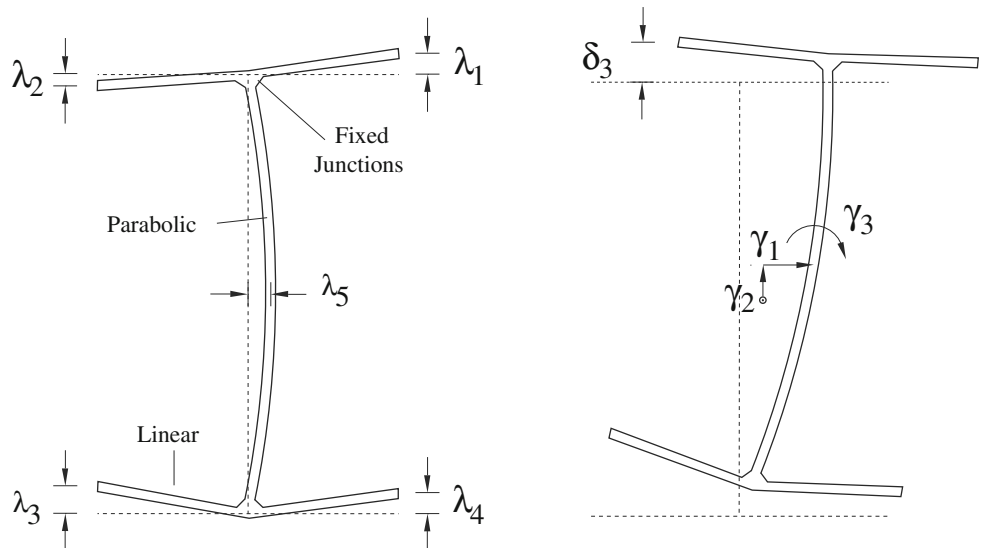
$$A_{l,n} = \sqrt{2 \cdot \tilde{S}_l(\omega_n, x) \cdot \Delta\omega} \tag{7b}$$

where $\Delta\omega = 3 \cdot 10^4$ rad/mm and parameters i, n and ϕ are analogous to Eq. (3). The complete geometric profile at each longitudinal position x is obtained by mapping the initial perfect cross-sectional geometry (y, z) to the imperfect cross-sectional geometry (Y, Z) in the form

$$\begin{aligned} \begin{bmatrix} Y \\ Z \end{bmatrix} &= \begin{bmatrix} y \\ z \end{bmatrix} + \alpha \cdot \left(\underbrace{\begin{bmatrix} 0 \\ \lambda_k \cdot \frac{|2y|}{B} \end{bmatrix}}_{\text{local components}} + \begin{bmatrix} \lambda_5 \cdot \left(1 - \left(\frac{2z}{D-t} \right)^2 \right) \\ 0 \end{bmatrix} \right) \\ &+ \underbrace{\begin{bmatrix} \gamma_1 \\ \gamma_2 \end{bmatrix}}_{\text{global components}} + \begin{bmatrix} \cos \gamma_3 & -\sin \gamma_3 \\ \sin \gamma_3 & \cos \gamma_3 \end{bmatrix} \cdot \begin{bmatrix} y \\ z \end{bmatrix} \end{aligned} \tag{8}$$

where B, D and t denote flange width, section height and plate thickness of the I-section according to Fig. 1, and α is a parameter that controls the magnitude of the imperfections. For $\alpha = 1$, amplitudes and spatial correlation of Eq. (8)

Fig. 5 Conceptual model for geometric imperfections. **a** The five local components λ at the flange edges and the web center (left side). **b** The three global components γ (right side)



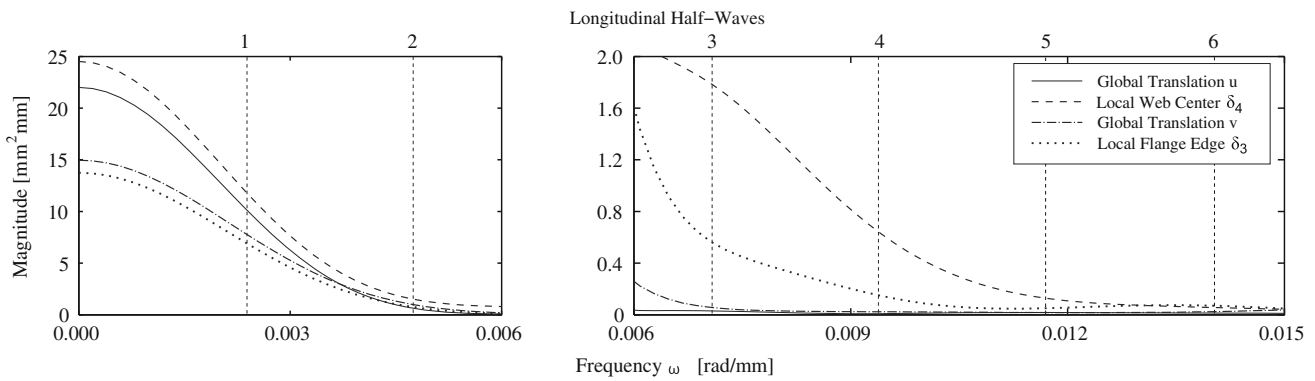


Fig. 6 Homogeneous periodograms of some global and local measurements. Global and local frequency ranges are separated at a half-wave number of 2.5. The power spectra of δ_3 and δ_4 in the frequency range

[0.006; 0.015] characterize corresponding local imperfection models δ_2 and δ_5

correspond to the imperfection measurements. By increasing $\alpha > 1$, the amplitudes of the imperfection samples are magnified, which is later used to illustrate the sensitivity of buckling behaviour of the I-section to the magnitude of geometric imperfections. The flange index in $\lambda_k, k = 1 \dots 4$ has to be chosen according to the current flange position of (y, z) .

longitudinal member axis, whereas the lowest local buckling mode consists of already 4 half-waves. Therefore, the frequency axis is partitioned into two distinct frequency bands

$$\omega_{global} = (0.000; 0.006) \text{ [rad/mm]} \tag{10a}$$

$$\omega_{local} = (0.006; 0.100) \text{ [rad/mm]} \tag{10b}$$

3.3 Measurement based power spectra for geometric imperfections

All spectrum values in the derived local and global power spectra, which are located outside the local or global frequency ranges ω_{local} and ω_{global} , respectively, are neglected in Eqs. (6) and (7), so that local imperfection samples lack the global frequencies and vice versa. According to Eq. (9), the limit $\omega = 0.006$ rad/mm represents 2.5 half-waves, so that local and global ranges contain the critical imperfection frequencies for local and global buckling, respectively. Figure 6 shows homogeneous periodograms of some local and global imperfections, each evaluated from the corresponding series of six measurements. They illustrate the typical frequency content of local and global imperfection measurements and its separation according to half-wave numbers n_{hw} of Eq. (9) and local and global frequency ranges according to Eqs. (10a) and (10b), respectively. It can be observed that frequencies larger than $\omega = 0.015$ rad/mm have a comparatively small contribution to the power spectrum. However, a conservative upper cut-off frequency in the local range ω_{local} is assumed to be $\omega = 0.1$ rad/mm.

Despite the analogy between experimental measurements and imperfection model, power spectra directly obtained from experimental data are inaccurate, because imperfection measurements comprise both local and global components. This is illustrated in Fig. 5 by comparing the measured flange imperfection λ_3 with its purely local counterpart λ_2 of the conceptual model, which are completely different.

According to experiments [18] as well as design guidelines [16,47], local and global geometric imperfection components in I-sections consist of small-scale, short-wave local oscillations and long-wave global oscillations with much larger amplitudes. It is therefore assumed in this work that the imperfection measurements can be separated in the frequency domain ω into two distinct parts, containing smaller local wave-lengths and larger global wave-lengths. Since imperfections in the form of Eigenmodes of the perfect structure have potentially the most decisive influence [8,10,18,47], it is sufficient to separate the critical local and global wave-lengths that correspond to a local or global buckling mode of the perfect I-section member. Buckling mode shapes occur in the present case in the form of longitudinal half-waves (see Sect. 4.1), whose number n_{hw} as a function of frequency ω can be calculated by

$$n_{hw} = \frac{\omega \cdot L_0}{\pi} \tag{9}$$

$$\hat{\phi}(x_k) = \frac{1}{2n + 1} \sum_{m=-n}^n \phi(x_{k+m}) \tag{11}$$

where $L_0 = 1330$ mm is the free length of the member. The global Euler modes comprise at most 2 half-waves along the

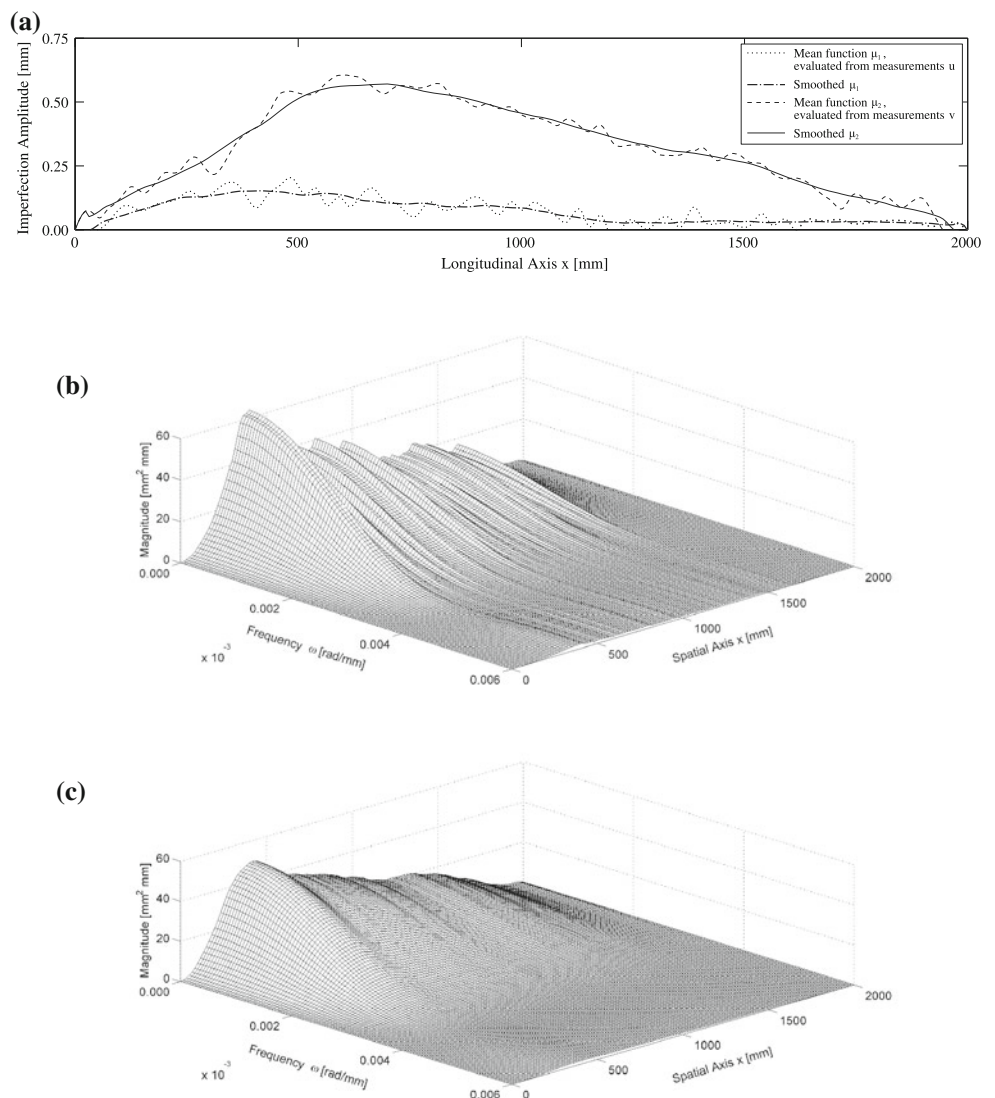
where ϕ and $\hat{\phi}$ are the initial and smoothed quantity, represented by discrete sample points x_k in space. Eq. (11) can

Fig. 7 Examples of computed mean functions and evolutionary power spectra for global imperfections γ .

a Initial and smoothed mean functions μ of global translational imperfections, evaluated by ensemble averaging and the smoothing algorithm Eq. (11).

b Evolutionary power spectrum for the zero-mean part of global weak axis translation γ_l , evaluated by the method of separation Eq. (2).

c Final evolutionary power spectrum for γ_l after smoothing with Eq. (11)



be seen as a moving window with empirical window size $2n + 1$, which successively replaces the central value by the arithmetic average of all visible values. The computed mean values and evolutionary power spectra sampled at 2^9 equally spaced discrete points x_k are smoothed with $n = 20$. Some examples of the initial and smoothed mean functions of the global translational imperfections as well as of computed evolutionary power spectra of the global weak axis translation γ_l , are shown in Fig. 7. Figure 8 illustrates typical local homogeneous flange and web imperfections, global non-homogeneous translations and cross-sectional rotation as well as the complete geometric imperfection profile.

3.4 Thickness imperfection model

For thickness imperfections, only mean μ_t and standard deviation σ_t are available (see Sect. 3.1), but no correlation

information that describes the spatial thickness variability. Therefore, the standard approach assuming the spatial variability in the form of the lowest perfect local Eigenmode is applied, which consist of four longitudinal half-waves. With Eq. (3) in mind, thickness samples $t^{(i)}$ are obtained as

$$t^{(i)} = \mu_t + \beta \cdot \sqrt{2}\sigma_t \cos(\omega_4 x + \phi_i) \tag{12}$$

with

$$S_4 = \frac{\sigma_t^2}{2\Delta\omega} \tag{13a}$$

$$\omega_4 = \frac{4 \cdot 2\pi}{L_0} \tag{13b}$$

$$\Delta\omega \rightarrow 0 \tag{13c}$$

where L_0 denotes the free length of the column. The parameter β is a scale factor analogous to α of Eq. (8) which is used later to examine the thickness imperfection sensitivity

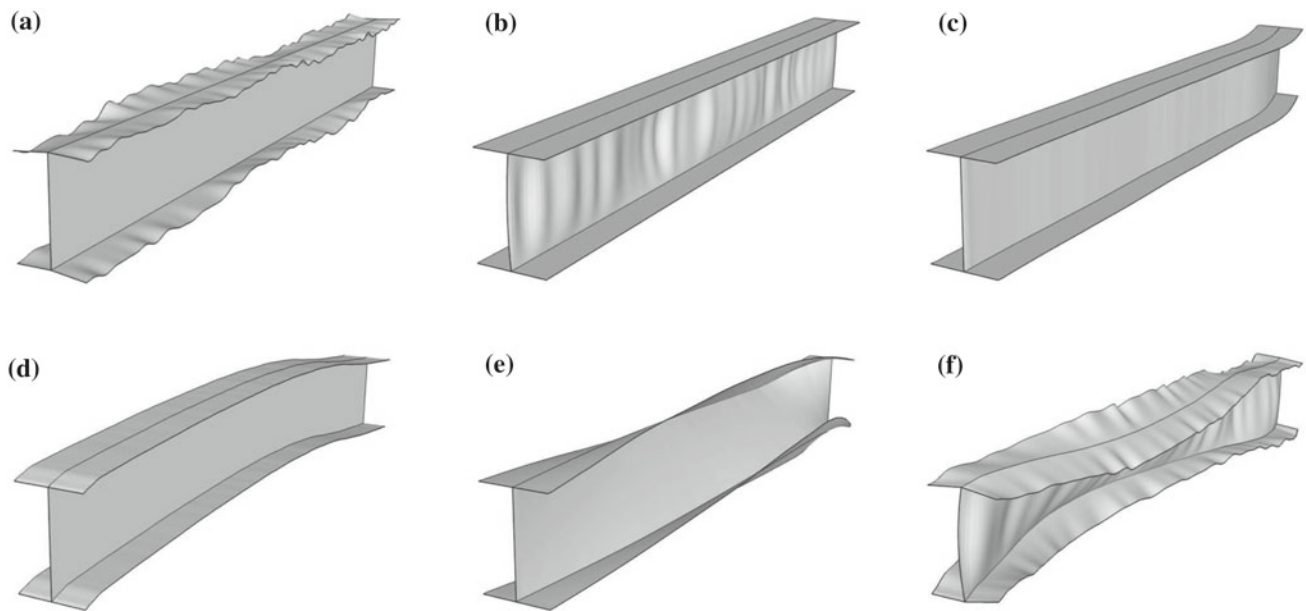


Fig. 8 Typical I-section samples with local and global geometric imperfections (80x enlarged). **a** Flange Imperfection λ_1 – λ_4 . **b** Web Imperfections λ_5 . **c** Weak Axis Translation γ_1 . **d** Strong Axis Translation γ_2 . **e** Cross-Sectional Rotation γ_3 . **f** Complete Profile Eq. (8)

of the I-section. Each sample $t^{(i)}$ is characterized by a single random variable ϕ_i , which generates a uniformly distributed phase shift. Since the width of the I-section plate components is several times smaller than their longitudinal length, thickness variation in space is assumed to be far more pronounced along the longitudinal I-section axis than in the transverse direction. Thickness imperfections are therefore modeled as a one-dimensional random field along the longitudinal axis in each of the three plate components. Three realizations of the random field—one for each flange and one for the web—are thus necessary for one I-section sample with imperfect thickness.

3.5 Boundary conditions

The I-section model takes into account the free-length part of I-section samples starting at position x' (see Fig. 1c), for which appropriate boundary conditions at the interface between stiffened and free-length parts have to be enforced.

Displacement boundary conditions: Due to the perfect pins at the member ends, rotations about the major y -axis and translations along the x -axis are left unconstrained. According to [19], rotations about the minor z -axis are constrained. Due to additional stiffeners and plates, rotations about the longitudinal axis and translations along the y -axis are prevented. The central web points at both boundaries are constrained against z -axis translations, and the central web point at one boundary against x -axis translation.

Applied forces: Forces at the interface boundaries resulting from the compression and bending jacks (see Fig. 2) are transferred to equivalent stresses in x -direction, however, always with respect to the perfect plate thickness. These forces are increased via the arc-length nonlinear algorithmic procedure [13]. Furthermore, the effect of the weight of the I-section member and half of the moment actuator bracings and levers is considered by applying equivalent displacements in y -direction, calculated beforehand according to Euler–Bernoulli beam theory.

4 Discretization with stochastic finite elements

Some central issues of the finite element discretization of the perfect geometry and the random field based imperfection models are shortly addressed here.

4.1 Discretization of the perfect structure

As illustrated in Fig. 9a, the I-section member is discretized by approximate squares, each of which consists of a pair of triangular TRIC shell elements. The deterministic constitutive law is isotropic Von Mises plasticity without hardening. Each element consists of 6 layers, which guarantee gradual through-the-thickness plastification. The additional axial stiffness and moments of inertia due to the welding material is compensated by overlapping of the web-flange junction elements and by slightly increasing their thicknesses (see Fig. 9b). Experiments show that web-flange junctions

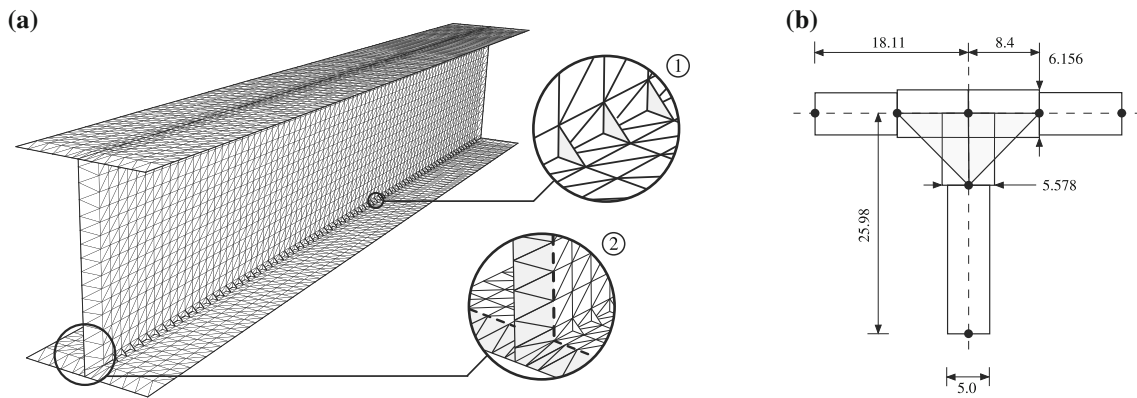


Fig. 9 Finite Element Discretization of the Free-Length Part. **a** Zoom 1 Position of membrane elements (grey-shaded). Zoom 2 Grey-shaded elements implement the warping stiffness. The boundary condi-

tions are imposed at the dashed line. **b** Discretization of the flange-web junctions. Membrane elements are grey-shaded

Fig. 10 Buckling in I-sections: Global flexural-torsional and local flange-web modes. **a** Global Flexural Mode. **b** Global Torsional Mode. **c** Primary Local Mode. **d** Secondary Local Mode

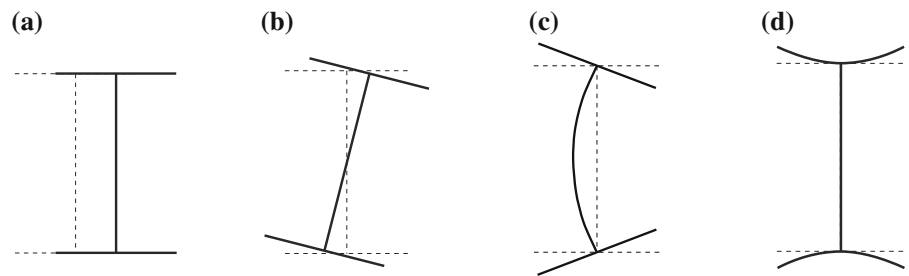
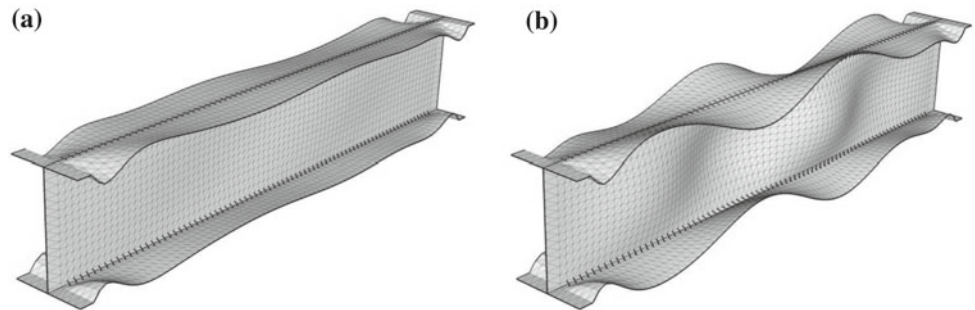


Fig. 11 Deformation at failure of the perfect structure. Out of plane deformations are magnified. **a** Elastic pre-buckling deformation. **b** 1st buckling mode



remain unaffected by local buckling deformations [19]. This is achieved by applying displacement constraints between the outer junction nodes with two very stiff TRIC membrane elements (see Fig. 9a, b). These elements are not allowed to bend and thus cannot interact along the longitudinal axis. Since at the interface between free and stiffened parts, the out-of-plane distortion of the cross-section is fully restrained in the reaction frame (see Figs. 1 and 2), the development of normal stresses due to warping in the flanges have to be ensured in the finite element model. This is accomplished by introducing some warping stiffness via an additional layer of very stiff TRIC elements placed at both ends behind the interface boundaries (see Fig. 9a). The effect of these virtual stubs is restricted to giving resistance against in-plane distortion and does not influence the above defined boundary conditions.

The buckling failure of typical I-section beam-columns constitutes a very complex process, which consists either of local web and flange buckling, global flexural and torsional buckling (see Fig. 10), or the interaction of several of these buckling phenomena [10, 17]. Due to its short length of 1330 mm, the stability behavior of the chosen example member is exclusively governed by the primary local mode shown in Fig. 10c, with various numbers of half-waves in longitudinal axis direction (see Fig. 12). The clearly pre-defined local failure phenomenon of the chosen short I-section member facilitates a detailed assessment of the impact of the random field based imperfection and the verification of the resulting buckling simulation. The elastic pre-buckling deformation and the perfect 1st mode shape as well as the axial load-displacement diagram of the perfect structure and characteristic

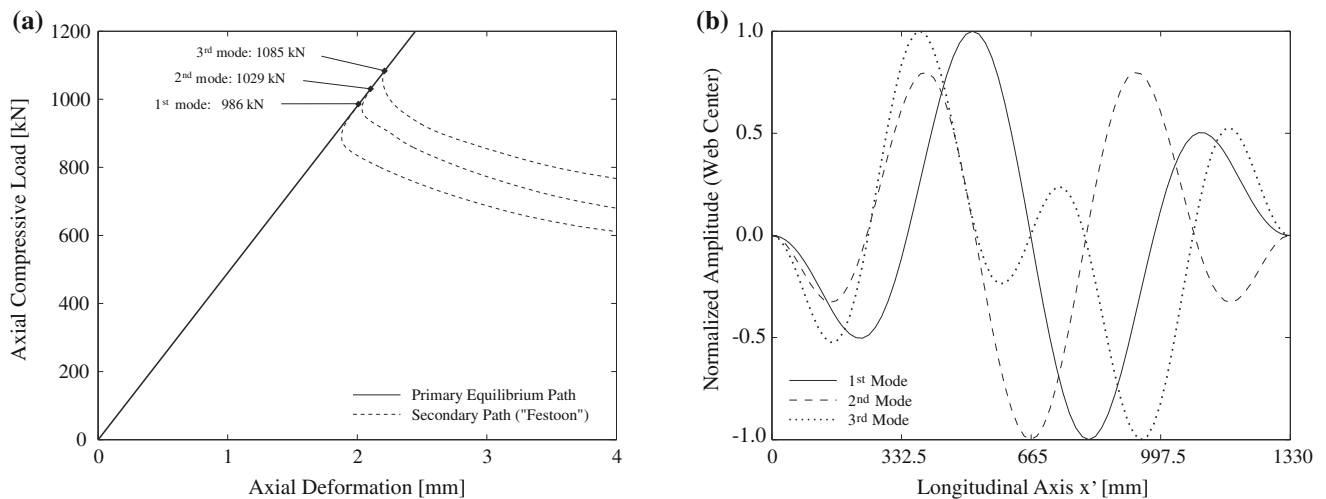


Fig. 12 Buckling response of the perfect structure under axial compression. **a** Axial load-displacement response. **b** Normalized web center displacements at failure

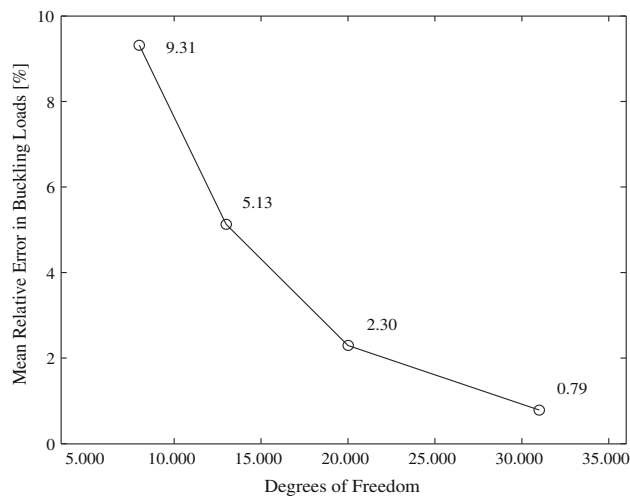


Fig. 13 Convergence study for the effective mesh density

half-waves of the first three perfect modes are shown in Figs. 11 and 12, respectively. The secondary paths in the post-buckling regime exhibit the typical festoon shape frequently found in thin-walled shell structures [8, 9, 33]. The identified 1st perfect local buckling mode of half-wave length 332.5 mm is in good agreement with elastic finite strip analyses for the same I-section with a critical half-wavelength of 300 mm [21].

4.2 Discretization of the imperfect structure

The integration of the stochastic imperfection models into the finite element framework necessitates the discretization of the continuous random fields as well. Geometric imperfections are directly incorporated into the finite element mesh by the imperfect geometry of nodal coordinates. Thickness

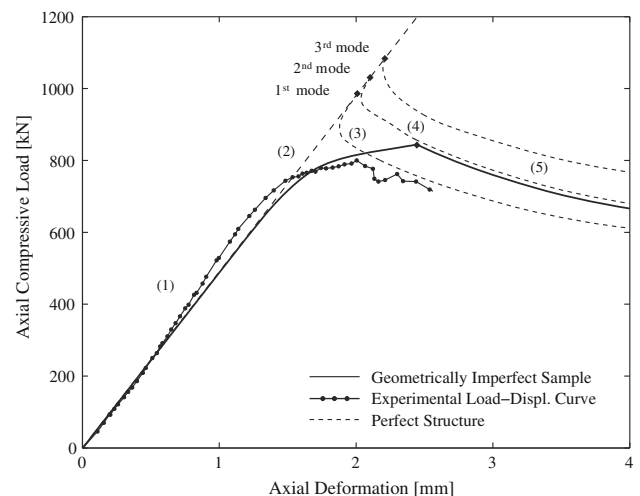


Fig. 14 Axial load-displacement response of a random geometrically imperfect sample compared to perfect and experimental response

imperfections are discretized by the midpoint method [45], which simply approximates the random field in each element by a single random variable defined as the value of the field at the triangle's centroid. The effect of the residual stresses is taken into account in each element by adding the residual stress components to regular stresses for the computation of the final stress state.

A suitable mesh density for the stochastic finite element model is chosen following a parametric convergence study. Fifty random geometrically imperfect samples are generated and corresponding ultimate buckling loads under axial compression are evaluated for five different mesh densities with approximately 8,000, 13,000, 20,000, 31,000 and 45,000 degrees of freedom, respectively. The average deviation of buckling loads from the results of the finest mesh is then

determined for all other discretizations as shown in Fig. 13. Accepting a potential mean error of around 2%, the third mesh size, also shown in Fig. 9a, with 3.404 nodes, 6.876 elements and 20.169 degrees of freedom is chosen for the subsequent numerical tests.

5 Stochastic buckling simulation of an imperfect I-section member

In this section, the results of the proposed methodology for the I-section beam-column are assessed in detail from theoretical, experimental and stochastic points of view.

5.1 Buckling of the geometrically imperfect column: theoretical and experimental points of view

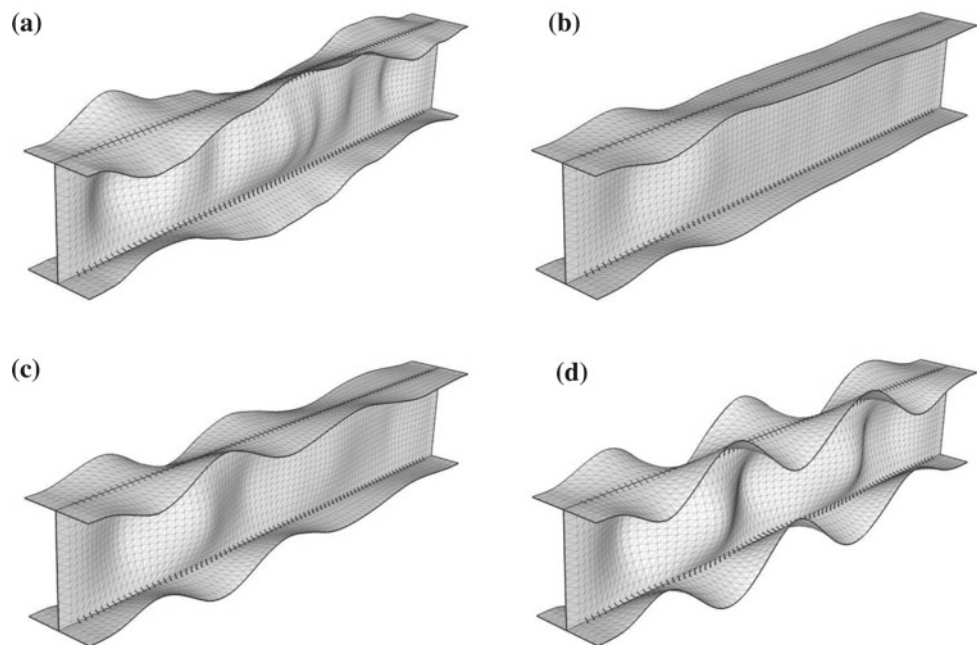
The influence of the geometric imperfection model is first investigated by monitoring axial load-displacement response and overall deformation of a single geometrically imperfect sample column under axial compression. Figure 14 shows the deviation of the experimental and computed imperfect non-linear load-displacement response from the corresponding perfect case. The gradual transition between ranges (1) and (3) of the response curve is characterized by the onset of local buckling (2). The non-linear range (3) is terminated by a bifurcation point (4), which represents the ultimate strength of the structure and is followed by the post-buckling regime (5).

The evolution of buckling is illustrated in Fig. 15 with some snapshots of the deformed structure. Due to their small

size, the critical deformations perpendicular to the web and flange plates are magnified by a factor ξ . Small non-linear deformations perpendicular to the plates are already present at early stages of the initial linear range, directly arising from the presence of geometric imperfections (see Fig. 15a). At the local buckling point (2), some parts of these non-linear deformations start to grow at an excessive rate, thus taking control of the overall deformation behaviour of the I-section member (see Fig. 15b, c). The final buckling mode at failure (Fig. 15d) gradually evolves from the imperfection triggered local buckle at the front end of the member, which corresponds to the elastic pre-buckling deformation in the perfect structure (see Fig. 15a). The failure mode exhibits local buckles in the form of five longitudinal half-waves, similar to the 2nd buckling mode of the perfect I-section (compare to Fig. 12b).

During the experiment, the I-section column specimen initially experienced local buckling of the flanges that led to the fast evolution of the typical half-waves along the complete length at ultimate strength (see Fig. 16). The slight unphysical increase in axial stiffness in the experimental load-displacement response in Fig. 14 is likely to be attributed to an unintended side-effect of the experimental set-up. The sensitive reaction of the examined finite element discretization to the presence of random field based imperfections in conjunction with the good agreement of load-displacement response and mode shapes with experiments suggests that the present methodology is able to predict the reduction and scattering of buckling loads in realistic conditions. Experimental as well as computed buckling response indicate that the examined medium-length I-section is moderately

Fig. 15 Snapshots from the deformation history of a random sample under axial compression. **a** $P = 600$ kN ($\xi = 250$): Imperfections determine pre-buckling shape. **b** $P = 782$ kN ($\xi = 25$): Onset of local buckling. **c** $P = 814$ kN ($\xi = 15$): Gradual evolution of 2nd mode from local buckle. **d** $P = 832$ kN ($\xi = 5$): Fully developed 2nd mode at ultimate strength



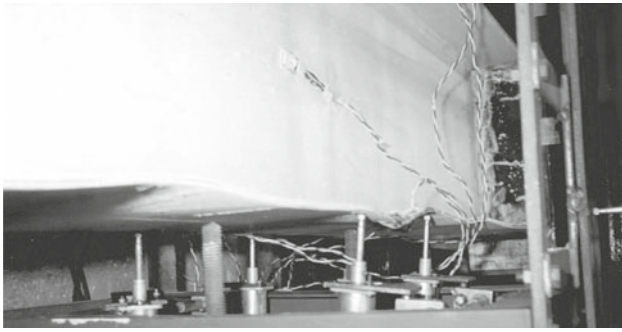


Fig. 16 Experimental failure in primary local buckling mode of I-section test specimen [19]

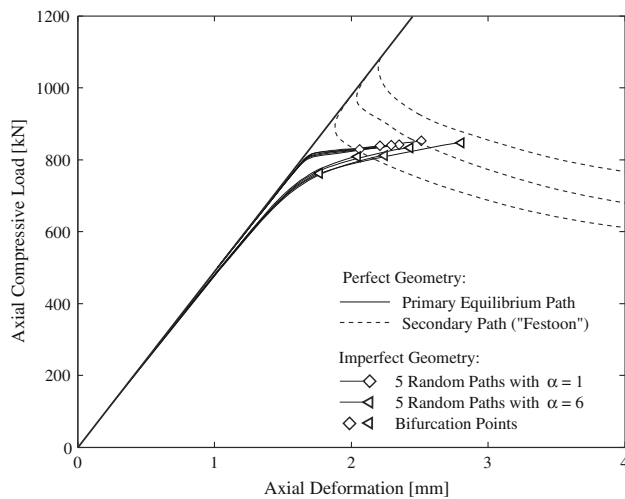


Fig. 17 Axial load-displacement response of two sets ($\alpha = 1$ and $\alpha = 6$) of imperfection levels for five random I-section samples under axial compression

imperfection sensitive as compared to highly sensitive structures such as thin shells, where the ultimate strength may be reduced more than 50% with respect to the perfect structure.

5.2 Buckling of the geometrically imperfect column: stochastic evaluation

In the following, the stochastic buckling behaviour of the discretized imperfect I-section example is evaluated by crude Monte-Carlo simulations (MCS). For each simulation, a non-linear finite element analysis is performed, while a sufficiently large number of I-section samples is considered in order to achieve convergence of second order response statistics. The non-linear finite element analyses are terminated after detection of the first negative Eigenvalue of the tangent stiffness matrix. The response variability of the load-displacement curves of five random samples under axial compression is plotted in Fig. 17. Triggered by imperfections, the imperfect equilibrium paths abandon the primary path and take a shortcut in the direction of the festoon shaped

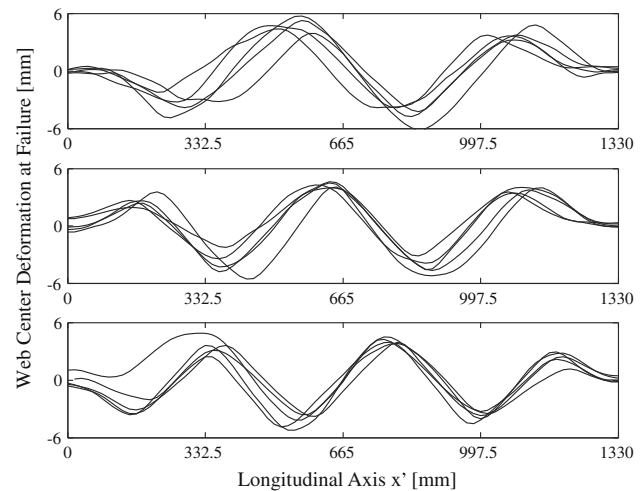


Fig. 18 Web center deformation at failure of five random samples, showing 4, 5 and 6 half-waves in the 1st, 2nd, and 3rd mode, respectively

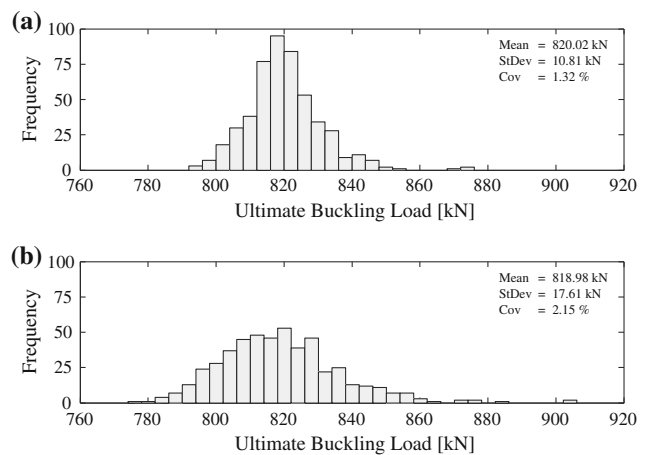


Fig. 19 Buckling load variability of 500 geometrically imperfect I-section samples. **a** Geometric imperfection level $\alpha = 1$. **b** Geometric imperfection level $\alpha = 3$

secondary paths of the perfect structure, which is a typical behaviour of imperfect shell and plate structures [8,9,33]. The buckling modes encountered in 500 simulations consist of 4, 5 or 6 longitudinal half-waves, respectively, as illustrated in Fig. 18. In contrast to the perfect modes in Fig. 12b, the imperfect modes are almost uniform in terms of amplitude and half-wave form.

The corresponding buckling load variability of the geometrically imperfect I-section member under axial load is shown in Fig. 19a. Its coefficient of variation of 1.3% is considerably lower than the corresponding variation of cylindrical shells, which was found around 8% [26]. The decrease in ultimate strength with respect to the first bifurcation point of the perfect structure amounts to 16.8 or 19.9% compared to the mean or the lowest encountered buckling load,

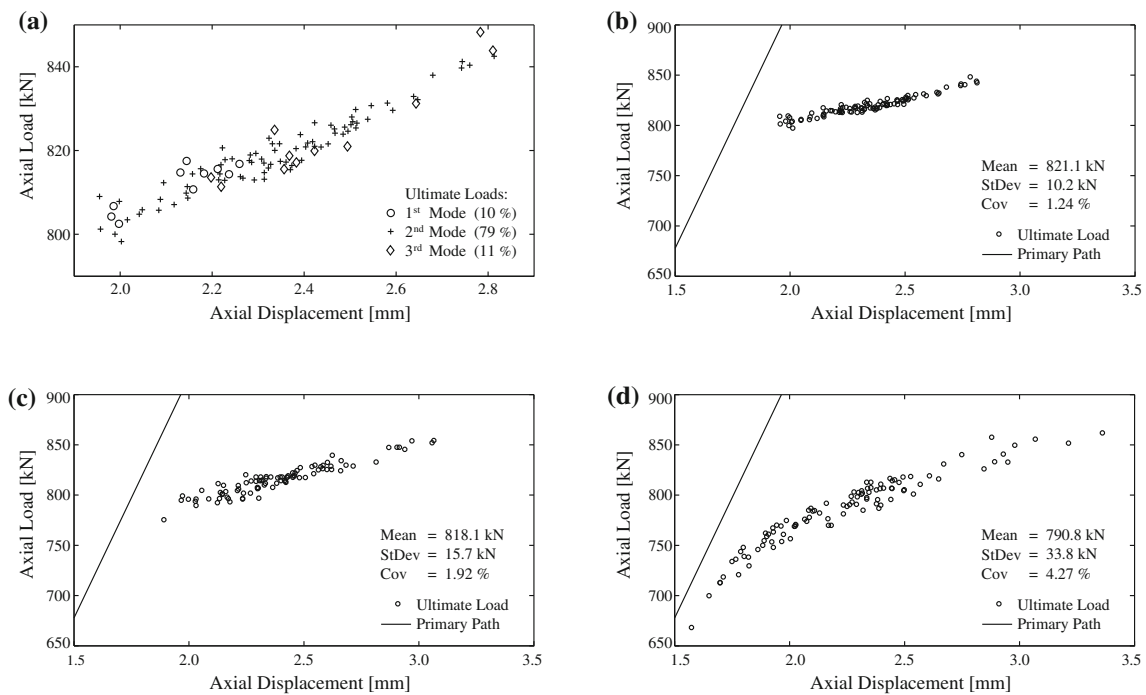


Fig. 20 Axial load-displacement response of 100 samples with varying geometric imperfection level α . **a** Half-wave numbers with $\alpha = 1$. **b** Failure points with $\alpha = 1$. **c** Failure points with $\alpha = 3$. **d** Failure points with $\alpha = 6$

respectively. For the same I-section column, a deterministic Eigenmode based geometric imperfection model gave a reduction of 24.1% [20,21], which verifies the generally conservative estimation of the standard Eigenmode approach.

5.3 Geometric imperfection sensitivity

The buckling load sensitivity under axial compression with respect to the amplitude of the complete geometric imperfection profile is tested by three sets of Monte Carlo simulations with 100 geometrically imperfect samples. While all sets use the same 100 local and global imperfection samples in Eqn. (8), each set corresponds to a different factor α of Eqn. (8). The change of load-displacement response for increasing geometric imperfection levels $\alpha = 1, 3, 6$ is illustrated in the scatter plots of Figs. 20b, c, d, respectively. The mean buckling load is shown to be marginally affected by the magnitude of geometric imperfections, represented by a slight decrease from 821 to 790 kN. The stochastic scattering of buckling loads, however, is strongly affected, represented by coefficients of variations up to 4.3% and a decrease in the lowest encountered buckling load from 798 to 668 kN. As shown in Fig. 17, equilibrium paths at increased geometric imperfections start to deviate from the primary perfect path at lower load levels and the failure points are distributed over a larger area in the load-displacement diagram, which leads to a larger scattering in buckling load histograms (Fig. 19a, b). For the same I-section, a similar parametric study has

been carried out with the standard Eigenmode based geometric imperfection model by increasing the amplitudes of the Eigenmodes [20]. It indicates that buckling loads under axial compression are completely insensitive to the level of geometric imperfections, which is similar to the mean buckling load behaviour of the random field based imperfection model, but fails to predict the dramatic increase in stochastic scattering. The difference in buckling response between the present random field based and the standard Eigenmode approach illustrates the importance of taking into account uncertainties in imperfection sensitivity studies for a comprehensive description of buckling phenomena.

5.4 Thickness imperfection sensitivity

Analogous to the previous section, the buckling load sensitivity with respect to the amplitude of thickness imperfections is tested by three sets of Monte Carlo simulations that differ in factor β , but use the same 100 random phase angles to produce thickness imperfection realizations in Eq. (12). Since thickness imperfections alone do not notably influence the buckling behaviour of the I-section discretization, they are combined with the geometric imperfection profiles of fixed $\alpha = 1$ that have been already used in the previous section. The comparison between Figs. 20a and 21a demonstrates that the combination of geometric imperfections with thickness imperfections leads to a considerable change of occurring mode shapes in terms of frequency and failure

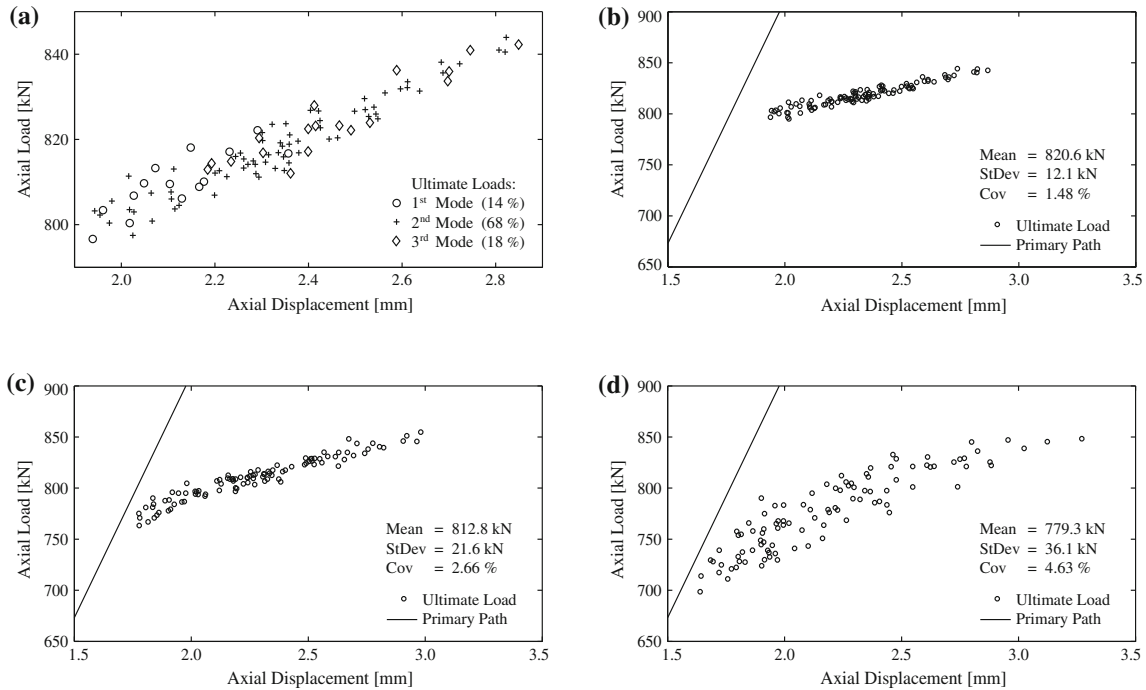


Fig. 21 Axial load-displacement response of 100 samples with combined geometric and thickness imperfections at constant level $\alpha = 1$ and varying levels β . **a** Half-wave numbers with $\alpha = 1$ and $\beta = 1$.

b Failure points with $\alpha = 1$ and $\beta = 1$. **c** Failure points with $\alpha = 1$ and $\beta = 3$. **d** Failure points with $\alpha = 1$ and $\beta = 6$

position in the load-displacement curve, which can be most likely traced back to mode interaction between geometric and thickness imperfections. The effects of the thickness amplitude variation by factor $\beta = 1, 3, 6$ on the buckling load variability are illustrated in Fig. 21b–d. Whereas the mean buckling load is again only slightly affected, the same increase in scattering encountered in Figs. 20b–d can be observed. It is remarkable that thickness imperfections, which do not have an effect when occurring alone, lead to a dramatic increase in buckling load variability comparable to a geometric imperfection level up to $\alpha = 6$.

5.5 Combined compression and major-axis bending: the stochastic interaction curve

The influence of combined loading on the ultimate strength of I-section members is typically illustrated by interaction curves [16,21,47] that show corresponding pairs of ultimate axial load and ultimate end moments for different load combinations. A stochastic interaction curve is derived for the present I-section column considering pure major axis bending M and pure axial compression P as well as 4 constant combinations: $M/P = 0.050, 0.125, 0.250$ and $0.500m$. In Fig. 22, the computed interaction curve of mean buckling loads is compared with the experimental buckling loads and the interaction formula according to Eurocode 3 [19,47]. The simulated curve has a convex shape,

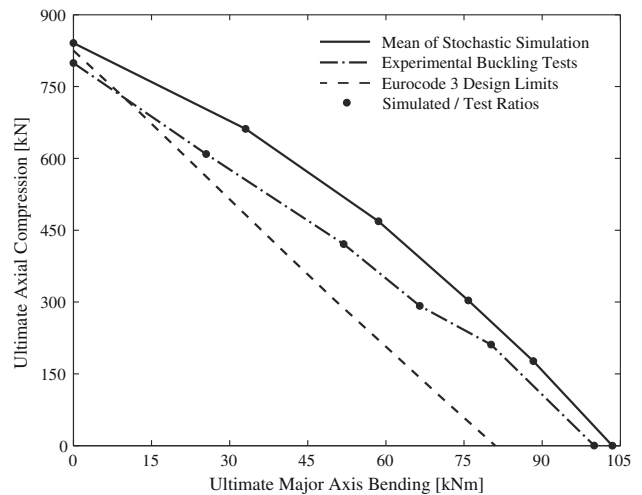


Fig. 22 Interaction curves for the I-section beam-column under various ratios of combined axial compression and major axis bending

which is confirmed in [21]. When compression is dominant the curve exhibits a slightly increased strength compared to experiments. This effect can be most likely attributed to the idealized boundary conditions at the interface between stiffened and free-length column parts, such as the complete restriction of rotations, which does not match exactly the boundary conditions of the experiments. The additional stochastic information of the simulated interaction curve is illustrated in Fig. 23 by adding a frequency dimension for the

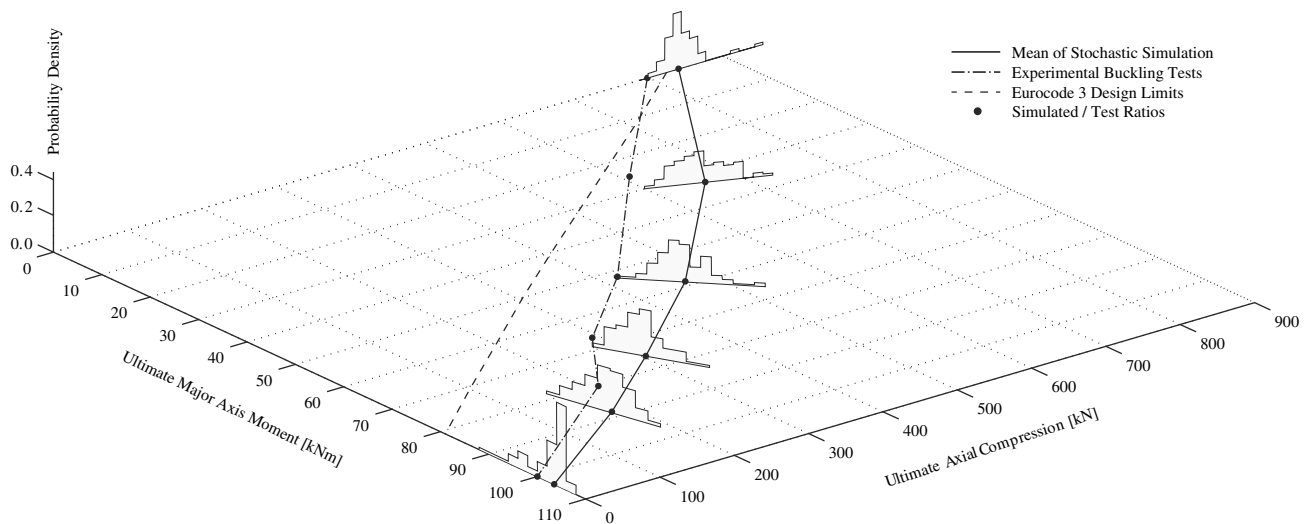


Fig. 23 Interaction curves for the I-section beam-column under various ratios of combined axial compression and major axis bending

representation of corresponding histograms. Each histogram was obtained with MCS using 100 I-section column samples. The EC3 curve, which has been derived on the basis of large scale experiments [18, 47], can be seen to be optimistic for pure compression, but becomes increasingly conservative with larger bending components. The stochastic interaction curve reproduces the characteristic buckling behaviour of the I-section beam-column as presumed by the EC3 curve. For dominating compression, the simulated histograms exhibit a positively skewed distribution with larger right tail. Thus, the simulated buckling loads do not scatter far below their mean value, which justifies the optimistic EC3 design rule for dominating compression. For dominating bending, however, the simulated histograms show a negatively skewed distribution with larger left tail. Thus, buckling loads must be expected to scatter far below their mean value, which requires a conservative rule in the EC3 curve.

6 Summary and conclusions

The present paper proposes a random fields approach for modeling geometric and thickness imperfections as the source of uncertainty for the buckling analysis of thin-walled I-section members. In particular, a geometric imperfection profile based on the spectral representation of local and global components is introduced, whose homogeneous and evolutionary power spectra can be directly calibrated from corresponding imperfection measurements. The random field based imperfection model of an I-section beam column is subsequently discretized with a detailed mesh of nonlinear shell finite elements and its stochastic buckling behaviour is evaluated by crude Monte-Carlo simulation. The potential of the proposed methodology to realistically simulate the reduction and variability of buckling loads is confirmed through

a number of numerical tests. It is shown that the resulting load-displacement response, buckling modes as well as stochastic key parameters and histograms reflect key concepts of imperfection triggered buckling and agree very well with corresponding experimental tests. It is illustrated that the proposed methodology offers the possibility of further insight in buckling related research and applications, among them the expansion of a small number of expensive and laborious buckling experiments by a large number of inexpensive virtual experiments, or advanced sensitivity studies that provide better conceptual understanding of physical mechanisms involved in the intricate failure process of thin-walled structures.

Acknowledgements Extensive research reports related to buckling experiments in I-sections have been kindly provided by Prof. Kim Rasmussen from the University of Sydney and Dr. Andreas Lechner from the Technical University of Graz. During his stay at NTU Athens, the first author has been partially supported by the German Academic Exchange Service (Deutscher Akademischer Austausch Dienst) and the German National Academic Foundation (Studienstiftung des deutschen Volkes). All support is gratefully acknowledged.

References

1. Argyris J, Tenek L, Olofsson L (1997) TRIC: a simple but sophisticated 3-node triangular element based on 6 rigid body and 12 straining modes for fast computational simulations of arbitrary isotropic and laminated composite shells. *Comput Methods Appl Mech Eng* 145:11–85
2. Argyris J, Tenek L, Papadrakakis M, Apostolopoulou C (1998) Postbuckling performance of the TRIC natural mode triangular element for isotropic and laminated composite shells. *Comput Methods Appl Mech Eng* 145:11–85
3. Argyris J, Papadrakakis M, Apostolopoulou C, Koutsourelakis S (2000) The TRIC shell element: theoretical and numerical investigation. *Comput Methods Appl Mech Eng* 166:211–231

4. Argyris J, Papadrakakis M, Stefanou G (2002) Stochastic finite element analysis of shells. *Comput Methods Appl Mech Eng* 191:4781–4804
5. Argyris J, Papadrakakis M, Karapitta L (2002) Elastoplastic analysis of shells with the triangular element TRIC. *Comput Methods Appl Mech Eng* 191(33):3613–3637
6. Basudhar A, Missoum S (2009) A sampling-based approach for probabilistic design with random fields. *Comput Methods Appl Mech Eng* 189(47–48):3647–3655
7. Blyfield MP, Nethercot DA (1997) Material and geometric properties of structural steel for use in design. *Struct Eng* 75(21):1–5
8. Budiansky B (1974) Theory of buckling and post-buckling behavior of elastic structures. In: *Advances in applied mechanics*, vol 14. Academic Press, New York, pp 1–65
9. Bushnell D (1985) *Computerized buckling analysis of shells*. Springer, New York
10. Bazant ZP, Cedolin L (1991) *Stability of structures: elastic, inelastic, fracture, and damage theories*. Kluwer, Dordrecht
11. Chen N-Z, Guedes Soares C (2008) Spectral stochastic finite element analysis for laminated composite plates. *Comput Methods Appl Mech Eng* 197:4830–4839
12. Craig KJ, Roux WJ (2008) On the investigation of shell buckling due to random geometrical imperfections implemented using Karhunen-Loève expansions. *Int J Numer Methods Eng* 73:1715–1726
13. Crisfield MA (1997) *Non-linear finite element analysis of solids and structures*, vol 1+2. Wiley, New York
14. Deodatis G, Spanos PD (eds) (2006) *Computational stochastic mechanics*. In: *Proceedings of the 5th International conference on computational stochastic mechanics (CSM-5)*, IOS Press, Amsterdam
15. Elishakoff I (2000) Uncertain buckling: its past, present and future. *Int J Solids Struct* 37:6869–6889
16. Galambos T (1998) *Guide to stability design criteria for metal structures*. Wiley, New York
17. Godoy LA (1999) *Theory of elastic stability: analysis and sensitivity*, Taylor and Francis, London
18. Greiner R, Kettler M, Lechner A, Freytag B, Linder J, Jaspert J-P, Boissonnade N, Bortolotti E, Weynand K, Ziller C, Oerder R (2008) *Plastic member capacity of semi-compact steel sections - a more Economic Design*, Final Report, European Research Fund for Coal and Steel
19. Hasham AS, Rasmussen KJR (1997) *Member capacity of thin-walled I-sections in combined compression and major axis bending*, Research Report No R746, School of Civil Engineering, University of Sydney
20. Hasham AS, Rasmussen KJR (2001) *Nonlinear analysis of locally buckled I-section steel beam-columns*. In: Zaras J, Kowal-Michalska K, Rhodes J (eds) *Thin-walled structures—advances and developments*, Proc. 3rd Int. Conf. on thin-walled structures, Elsevier, Krakow, pp 427–436
21. Hasham AS, Rasmussen KJR (2002) *Interaction curves for locally buckled I-section beam-columns*. *J Constr Steel Res* 58:213–241
22. Kala Z (2005) *Sensitivity analysis of the stability problems of thin-walled structures*. *J Constr Steel Res* 61(3):415–422
23. Kolanek K, Jendo S (2008) *Random field models of geometrically imperfect structures with “clamped” boundary conditions*. *Probab Eng Mech* 23(2):219–226
24. Newland DE (1993) *An introduction to random vibrations, spectral and wavelet analysis*. Wiley, New York
25. Papadopoulos V, Papadrakakis M (2004) *Finite element analysis of cylindrical panels with random initial imperfections*. *J Eng Mech* 130:867–876
26. Papadopoulos V, Papadrakakis M (2005) *The effect of material and thickness variability on the buckling load of shells with random initial imperfections*. *Comput Methods Appl Mech Eng* 194:1405–1426
27. Papadopoulos V, Igleis P (2007) *The effect of non-uniformity of axial loading on the buckling behaviour of shells with random imperfections*. *Int J Solids Struct* 44:6299–6317
28. Papadopoulos V, Charnpis DC, Papadrakakis M (2008) *A computationally efficient method for the buckling analysis of shells with stochastic imperfections*. *Comput Mech* 43:687–700
29. Papadopoulos V, Stefanou G, Papadrakakis M (2009) *Buckling analysis of imperfect shells with stochastic non-Gaussian material and thickness properties*. *Int J Solids Struct* 46:2800–2808
30. Papoulis A, Pillai SU (2002) *Probability, random variables and stochastic processes*. McGraw-Hill, New York
31. Priestley MB (1981) *Spectral analysis and time series*. Academic Press, London
32. Priestley MB (1988) *Nonlinear and non-stationary time series analysis*. Academic Press, London
33. Ramm E, Wall W (2004) *Shell structures. A sensitive interrelation between physics and numerics*. *Int J Numer Methods Eng* 60:381–427
34. Rasmussen KJR, Hancock GJ (2000) *Buckling analysis of thin-walled structures: numerical developments and applications*. *Prog Struct Eng Mater* 2(3):359–368
35. Schafer BW, Grigoriu M, Peköz T (1998) *A probabilistic examination of the ultimate strength of cold-formed steel elements*. *Thin Walled Struct* 31:271–288
36. Schenk CA, Schuëller GI (2003) *Buckling analysis of cylindrical shells with random geometric imperfections*. *Int J Non Linear Mech* 38:1119–1132
37. Schenk CA, Schuëller GI (2005) *Uncertainty assessment of large finite element systems*, Lecture Notes in applied and computational mechanics, vol. 24, Springer, Berlin
38. Schenk CA, Schuëller GI (2007) *Buckling analysis of cylindrical shells with cutouts including random boundary and geometric imperfections*. *Comput Methods Appl Mech Eng* 196:3424–3434
39. Schillinger D, Papadopoulos V (2010) *Accurate estimation of evolutionary power spectra for strongly narrow-band random fields*. *Comput Methods Appl Mech Eng* 199(17–20):947–960
40. Shinozuka M, Deodatis G (1991) *Simulation of stochastic processes by spectral representation*. *Appl Mech Rev (ASME)* 44:191–203
41. Shinozuka M, Deodatis G (1996) *Simulation of multi-dimensional Gaussian stochastic fields by spectral representation*. *Appl Mech Rev (ASME)* 49:29–53
42. Stefanou G, Papadrakakis M (2004) *Stochastic finite element analysis of shells with combined random material and geometric properties*. *Comput Methods Appl Mech Eng* 193:139–160
43. Stefanou G, Papadrakakis M (2007) *Assessment of spectral representation and Karhunen-Loève expansion methods for the simulation of Gaussian stochastic fields*. *Comput Methods Appl Mech Eng* 196:2465–2477
44. Stefanou G (2009) *The stochastic finite element method: past, present and future*. *Comput Methods Appl Mech Eng* 198:1031–1051
45. Sudret B, Der Kiureghian A (2000) *Stochastic finite element methods and reliability: a state-of-the-art report*, Rep. No. UCB/SEMM-2000/08, University of California at Berkeley, USA
46. Tootkaboni M, Graham-Brady L, Schafer BW (2009) *Geometrically non-linear behavior of structural systems with random material property: an asymptotic spectral stochastic approach*. *Comput Methods Appl Mech Eng* 198:3173–3185
47. Trahair NS, Bradford MA, Nethercot DA, Gardner L (2008) *The behaviour and design of steel structures to EC3*, Taylor and Francis, London
48. Vanmarcke E (1983) *Random fields analysis and synthesis*. The MIT Press, MA, Cambridge